buildings

MDPI

Article

Analytical Derivation of the q-Factor for Slender Masonry Structures Under Out-of-Plane Seismic Action

Simona Coccia

Department of Civil Engineering and Computer Science Engineering, University of Rome "Tor Vergata", Via del Politecnico 1, 00133 Rome, Italy; coccia@ing.uniroma2.it

Abstract

Slender masonry structures, in the absence of disintegration phenomena, can be idealized as rigid bodies subjected to seismic excitation. In this study, a closed-form expression for the behavior factor (*q*-factor) associated with overturning collapse under out-of-plane seismic loading is derived. The analysis considers five-step pulse seismic inputs. In the proposed approach, valid for slender masonry structures, sliding failure is neglected, and collapse is assumed to occur when, at the end of the seismic excitation, the rotation of the structure reaches a value equal to its slenderness. Based on this criterion, it is possible to derive a formulation for the q-factor as a function of a dimensionless parameter that combines the geometric characteristics of the slender structure and the period of the applied accelerogram. To validate the proposed formulation, a comparative analysis is conducted against the results obtained from a numerical integration of the motion equation using a set of 20 natural accelerograms recorded in Italy. The characteristic period of each accelerogram is evaluated through different methodologies, with the aim of identifying the most suitable approach for application in simplified seismic assessment procedures.

Keywords: slender masonry structure; q-factor; earthquake period

Academic Editor: Gabriele Milani

Received: 25 June 2025
Revised: 16 July 2025
Accepted: 22 July 2025
Published: 24 July 2025

Citation: Coccia, S. Analytical Derivation of the q-Factor for Slender Masonry Structures Under Out-of-Plane Seismic Action. *Buildings* **2025**, *15*, 2622. https://doi.org/10.3390/buildings15152622

1. Introduction

The seismic behavior of unreinforced masonry structures—such as piers, statues, out-of-plane walls, and other slender structures—has been extensively studied in literature due to their high vulnerability to earthquake ground motions (see, for example, [1–4]). In the presence of poor mechanical properties and inadequate masonry detailing, collapse tends to occur through material disintegration. Conversely, when the masonry exhibits good mechanical characteristics, the structural response under out-of-plane actions is typically monolithic [5]. In such cases, cracking localizes, leading to the formation of distinct macro-elements. These slender masonry components can thus be idealized as undergoing rocking motion, where the structure behaves as one or more rigid bodies rotating about a predefined hinge. The concept of rocking was first formalized in the seminal work of Housner [6], who modeled a masonry structure as an inverted rigid pendulum subjected to horizontal ground acceleration. In this model, the coefficient of friction between the block and its base is assumed to be sufficiently high, allowing only rocking and uplift motions, while sliding is neglected. Housner's analysis demonstrated that masonry blocks do not necessarily collapse when subjected to seismic excitation; instead, they can remain stable without overturning, provided that the ground acceleration remains below a critical threshold determined by the block's geometry. Building on Housner's foundational work, subsequent studies have explored the dynamic response of masonry single-block

(e.g., [7–21]) or multi-block (e.g., [22–24]) columns. Yim et al. [7] introduced a probabilistic perspective on the rocking response of rigid blocks, highlighting that "the rocking response of a block is very sensitive to small changes in its size and slenderness ratio, and to the details of the ground motion". Their findings demonstrated that larger blocks tend to exhibit enhanced seismic stability. Similar deductions have been reported by many other authors (e.g., [8–10]). Makris and Roussos [11] revisited Housner's seminal work by examining the overturning behavior of electrical equipment subjected to near-fault ground motions. They refined the critical acceleration threshold for overturning under a half-sine pulse, showing that collapse occurs during the free vibration phase following the pulse—rather than at the pulse's peak—thus underscoring the importance of pulse duration alongside amplitude. Some studies investigated various overturning mechanisms, revealing that overturning may occur either through impact sequences or in a non-impact mode (e.g., [12–14]). Zhang and Makris [12] defined a stability domain in the acceleration–frequency plane, delineating the dynamic thresholds for overturning. Several researchers (e.g., [15–21]) have derived analytical closed-form solutions for overturning thresholds, offering critical insights into the dynamic stability limits of rocking systems. Housner's approach has also been adapted to more complex collapse mechanisms, such as those involving multi-storey regular masonry walls with openings (e.g., [25]), wall-restrained rocking (e.g., [26,27]), and masonry arches (e.g., [28–32]) and has been used to construct fragility curves (e.g., [33]). In a recent contribution, Nodargi and Bisegna [34] expanded this last framework to incorporate not only overturning but also sliding failure mechanisms. Recent studies have extended the classical Housner model to investigate the influence of horizontal restraints on the rocking behavior of rigid blocks [35], to analyze foundation effects [36], or to design base isolation systems for the seismic protection of rocking structures [37]. The use of the structure factor (q-factor) in the out-of-plane verification of masonry structures is fundamental to obtaining accurate and reliable seismic performance assessments. Neglecting the structure factor can result in overly simplified models that underestimate the actual demand or overestimate the capacity of masonry walls, leading to unsafe or excessively conservative design outcomes. Its appropriate application allows for a more realistic estimation of the seismic vulnerability of masonry structures and supports the development of efficient strengthening and retrofitting strategies in accordance with performance-based design principles.

In this study, a stability domain is defined in the (q-factor, $p{\cdot}t_o$) plane, where the q-factor represents the ratio between the collapse-inducing acceleration and the motion activation acceleration, p is the structural pulsation, and t_o is the half-period of the ground accelerogram. The proposed model is valid for slender elements, defined by a height-to-base ratio greater than 3 (i.e., slenderness $\alpha < 0.35$). For such values, under seismic excitation, the structural response is predominantly governed by rocking motion, and base sliding effects can be reasonably neglected [38]. The methodology follows and expands upon the approach proposed in [10] and [20] by considering five different idealized seismic inputs within Housner's rocking motion framework. In [10], a square-wave acceleration input is used to evaluate the collapse acceleration of a slender masonry block. This approach has been applied to the analysis of masonry restraint walls [26] and circular masonry arches [31]. Collapse is defined as the condition in which the block reaches a rotation equal to its slenderness at the end of the seismic input. Under this assumption, rotation increases without impact and without reversal of motion, characterizing a smooth transition into overturning without energy dissipation through impacts. In this paper, the same procedure is applied to a wider range of seismic input excitations. Finally, particular attention is devoted to the definition of the accelerogram's half-period t_o, which is a key parameter for developing a simplified and practical approach for the seismic safety verification of the out-of-plane response of slender masonry structures.

Various mathematical representations have been employed in the literature to approximate seismic inputs, ranging from constant or sinusoidal functions to more complex wavelet-based models (e.g., [39,40]). In this work, the period T_p and the corresponding half-period $t_o = T_p/2$ of each accelerogram are estimated using eleven different methodologies and using a set of 20 natural accelerograms recorded in Italy. The method yielding the most consistent and reliable results for seismic performance assessment is identified and adopted in the subsequent analyses.

2. Analytical Model

The reference structure considered is a slender masonry block resting on a rigid foundation and subjected to seismic ground motion. The geometric properties of the block are illustrated in Figure 1.

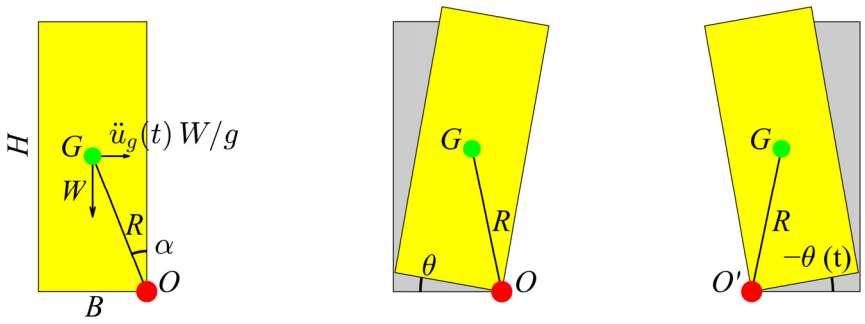

Figure 1. Reference masonry structure.

When subjected to an earthquake with a peak ground acceleration (*PGA*) exceeding the slenderness ratio α of the block, and assuming the structure behaves as rigid in compression with zero tensile strength—while neglecting sliding—the block initiates rocking motion about a base corner (point O or O' in Figure 1). Given a seismic input $\ddot{u}_g$, the rotation θ of the block can be evaluated by the differential equation originally derived by Housner [6]:

$$I_0\ddot{\theta} - WRsin(\alpha - \theta) = -WR\frac{\ddot{u}_g}{g}cos(\alpha - \theta) \tag{1}$$

where W is the weight, R the distance of the center of gravity G from the hinge O or O' (Figure 1), and I_o is the rotational moment around the hinge:

$$I_o = \frac{1}{3}\frac{W}{g}4H^2\left(1 + (tan\alpha)^2\right) \tag{2}$$

Considering small slenderness values ($\alpha < 0.25$), the equation of motion (1) is simplified to

$$\ddot{\theta} - p^2(\alpha - \theta) = -p^2\frac{\ddot{u}_g}{g} \tag{3}$$

where the pulsation p can be evaluated with the following well-known relationship:

$$p = \sqrt{\frac{WR}{I_0}} \tag{4}$$

The pulsation as a function of the geometric characteristics of the structure is shown in Figure 2.

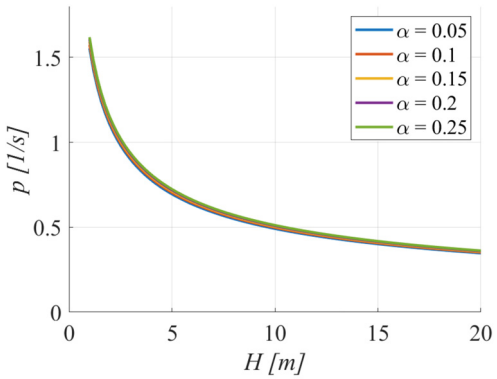

Figure 2. Pulsation as a function of block height.

The pulsation p is only weakly influenced by the slenderness of the block but strongly depends on its height. Taller blocks exhibit lower pulsation values, which, as will be discussed later, contributes to increased resistance to seismic excitation.

A closed-form solution for the rotation θ (i.e., the solution to the motion differential Equation (3)) can be obtained only when the seismic input is represented by a simple analytical function, such as a constant or a sinusoidal acceleration. In this study, five step-pulse ground accelerations are considered (Figure 2). For the block, rotational motion initiates when the horizontal ground acceleration reaches a value equal to $\alpha\, g$ (assuming $\alpha \approx \tan(\alpha)$), where g is the gravitational acceleration. At this point, the resultant force passes through the hinge at point O (or O'), triggering oscillation about that corner.

The structural behavior factor is defined as the ratio between the peak ground acceleration (PGA) that causes dynamic collapse of the block and the acceleration threshold that initiates rocking motion:

$$q = \frac{PGA}{\alpha g} \tag{5}$$

A subscript i for q (q_1 etc.) is later used to indicate the case of the seismic input (with i ranging from 1 to 5).

As in [6,10,20], the proposed model assumes that the block undergoes a rotation θ equal to its slenderness α at the end of the used seismic input ($t = t_{fin}$ in Figure 3). This assumption is justified by the fact that, in the real accelerogram, the direction of seismic excitation, after the end of the primary pulse, coincides with the direction of motion. Such alignment represents the worst-case scenario, potentially leading to rotations exceeding the slenderness ratio of the block. Then, this condition can be regarded as a state of unstable equilibrium.

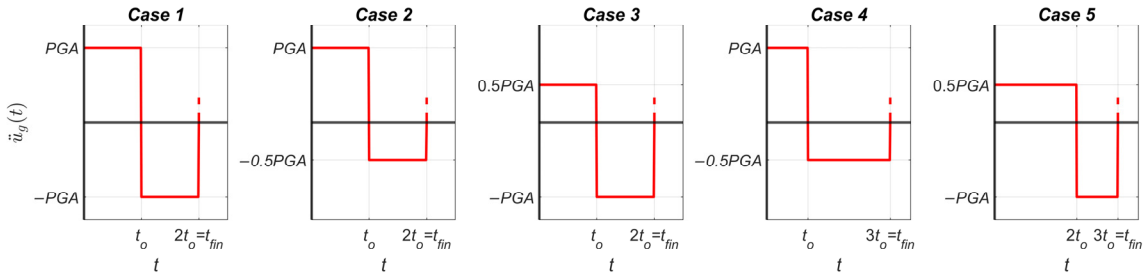

Figure 3. Ground acceleration input adopted in the model.

Applying Equation (3) to Case 1 in Figure 3 leads to the following relationship when $t < t_o$:

$$\ddot{\theta} + p^2(\alpha - \theta) = p^2 \frac{PGA}{g} \tag{6}$$

The rotation and angular velocity of the block at time t are derived by integrating Equation (6):

$$\theta(pt) = \alpha\left(\frac{PGA}{\alpha g} - 1\right)(cosh(pt) - 1) = \alpha(q_1 - 1)(cosh(pt) - 1) \tag{7}$$

$$\dot{\theta}(pt) = \alpha p\left(\frac{PGA}{\alpha g} - 1\right)(sinh(pt)) = \alpha p(q_1 - 1)(sinh(pt)) \tag{8}$$

At time t_o, the rotation $\theta(pt_o)$ and the angular velocity $\dot{\theta}(pt_o)$ of the block represent the initial conditions for the integration of the equation of motion for $t > t_o$, which is

$$\ddot{\theta} + p^2(\alpha - \theta) = -p^2\frac{PGA}{g} \tag{9}$$

The integration of Equation (9) gives the rotation of the block for $t > t_o$:

$$\theta(t) = 2\alpha\left[\left(sinh\left(\frac{pt}{2}\right)\right)^2(q_1 - 1) - 2q_1\left(sinh\left(\frac{p}{2}(t - t_o)\right)\right)^2\right] \tag{10}$$

Considering the collapse condition $\theta = \alpha$ at the end of the seismic input,

$$\theta(2t_o) = \alpha \tag{11}$$

the behavior factor is obtained:

$$q_1 = \frac{2(cosh(pt_o))^2 - 1}{2cosh(pt_o)(cosh(pt_o) - 1)} \tag{12}$$

Similarly, considering the second seismic input, the rotation and velocity for $t < t_o$ are given by Equations (7) and (8) (with q_2 replacing q_1), while for $t > t_o$, the equation of motion is

$$\ddot{\theta} + p^2(\alpha - \theta) = -p^2\frac{PGA}{2g} \tag{13}$$

And the rotation of the block for $t > t_o$

$$\theta(t) = \alpha\left[2\left(sinh\left(\frac{pt}{2}\right)\right)^2(q_2 - 1) - 3q_2\left(sinh\left(\frac{p}{2}(t - t_o)\right)\right)^2\right] \tag{14}$$

Considering Equation (11), the strength reduction factor becomes

$$q_2 = \frac{2 - 4(cosh(pt_o))^2}{3cosh(pt_o) - 4(cosh(pt_o))^2 + 1} \tag{15}$$

Considering the third seismic input, the rotation and angular velocity for $t < t_o$ are

$$\theta(t) = \alpha\left(\frac{q_3}{2} - 1\right)(cosh(pt) - 1) \tag{16}$$

$$\dot{\theta}(t) = \alpha p\left(\frac{q_3}{2} - 1\right)(sinh(pt)) \tag{17}$$

By integrating the equation of motion (Equation (9)), which applies for $t > t_o$, with the boundary conditions (Equations (16) and (17) at $t = t_o$), the rotation of the block is obtained:

$$\theta(t) = \alpha\left[\left(sinh\left(\frac{pt}{2}\right)\right)^2(q_3 - 2) - 3q_3\left(sinh\left(\frac{p}{2}(t - t_o)\right)\right)^2\right] \tag{18}$$

And the strength reduction factor producing the collapse of the block is

$$q_3 = \frac{4(cosh(pt_o))^2 - 2}{2(cosh(pt_o))^2 - 3cosh(pt_o) + 1} \tag{19}$$

Considering the fourth input, the equation of motion is given by Equation (6). Accordingly, the rotation and the angular velocity for $t < t_o$ are described by Equations (7) and (8), while for $t > t_o$, the equation of motion is given by Equation (13), which, when integrated with the boundary conditions, gives the rotation for $t > t_o$:

$$\theta(t) = \alpha \left[2\left(sinh\left(\frac{pt}{2} \right) \right)^2 (q_4 - 1) - 3q_4 \left(sinh\left(\frac{p}{2}(t - t_o) \right) \right)^2 \right] \tag{20}$$

Imposing the collapse condition

$$\theta(3t_o) = \alpha \tag{21}$$

provides

$$q_4 = \frac{2cosh(3pt_o)}{2cosh(3pt_o) - 3cosh(2pt_o) + 1} \tag{22}$$

Finally, considering the fifth input and following steps like the previous cases, the rotation for $t > 2t_o$ is

$$\theta(t) = \alpha \left[2\left(sinh\left(\frac{pt}{2} \right) \right)^2 (q_5 - 1) - 3q_5 \left(sinh\left(\frac{p}{2}(t - 2t_o) \right) \right)^2 \right] \tag{23}$$

and collapse is reached if

$$q_5 = \frac{2cosh(3pt_o)}{cosh(3pt_o) - 3cosh(pt_o) + 2} \tag{24}$$

Figure 4 shows the values of q for varying pt_o ratios. Clearly, for Cases 3 and 5, values of q less than 2 cannot be considered, as they would imply an initial acceleration below the threshold required to initiate rocking motion.

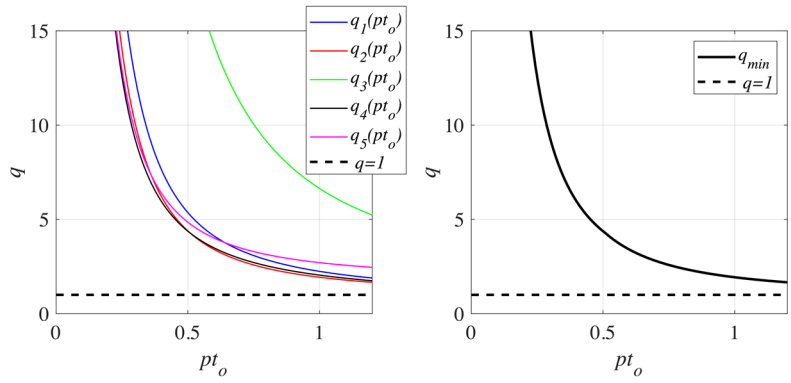

Figure 4. q-factor as a function of pt_o.

The same graph also indicates the minimum value of q, which corresponds to q_4 for $pt_o < 0.51$, and to q_2 for higher values of pt_o. To ensure a safety margin, the smallest value among all calculated q-factors must be adopted in the seismic analysis.

The expressions derived for the behaviour factor are valid only in the absence of impact during motion. In cases where an impact occurs, the governing differential equations can be solved either by using numerical integration methods—such as MATLAB's ODE45

solver [41]—or by identifying the time of impact and solving a new differential equation with a non-zero initial angular velocity.

In Figure 5, the results of numerical integration performed in MATLABR2024b are presented. The seismic inputs shown in Figure 3 are applied, with varying PGA intensity according to the following equation:

$$PGA = q_i \alpha g R_d \tag{25}$$

where R_d is a reduction coefficient (with $R_d < 1$) used to assess whether seismic inputs are lower than those predicted by the proposed q-factor.

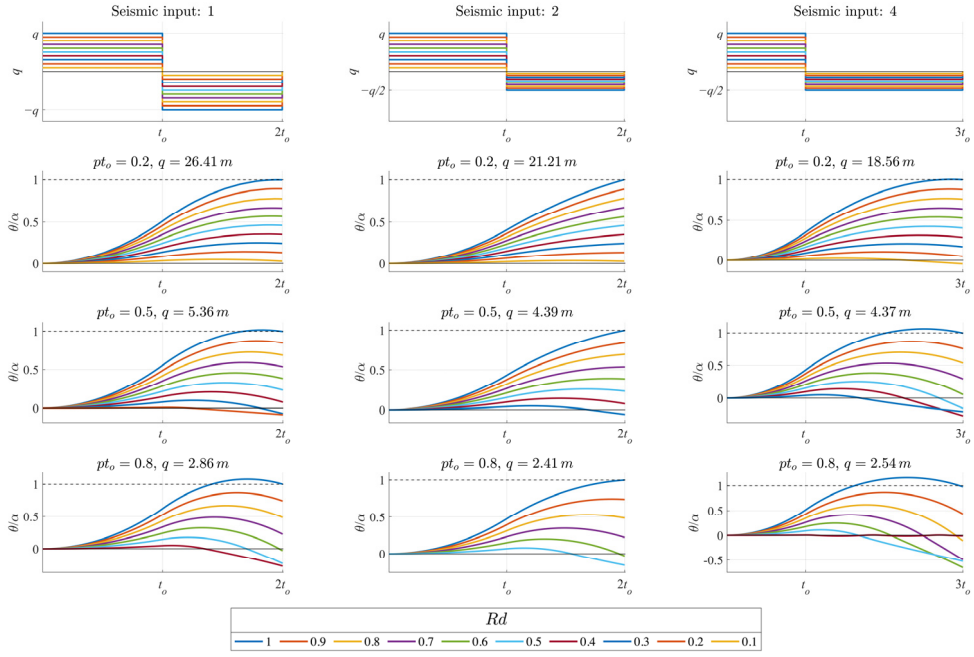

Figure 5. θ/α versus t for reduced seismic excitation.

The selected values of R_d must satisfy the condition

$$q_i R_d = \frac{PGA}{\alpha g} > 1 \tag{26}$$

otherwise, no rocking motion is initiated in the block. Energy dissipation due to the impact (e.g., [6–42]) is not considered in numerical investigation.

The cases analyzed concern seismic excitations represented by Cases 1, 2, and 4, for pt_o values ranging between 0.2 and 0.8. The pulsation p decreases as the height H of the block increases. Considering a minimum height H = 1 m, the maximum pulsation p reaches approximately 1.6 s^{-1}. Assuming a maximum half-period t_o = 0.5 s, the corresponding upper limit for pt_o is approximately 0.8. In Figure 5, the non-dimensional ratio θ/α is plotted against the non-dimensional parameter pt_o. In the cases analyzed, impact only occurs for low values of the coefficient R_d, and the resulting post-impact rotations remain limited. As observed in all the results obtained, collapse does not occur for $R_d < 1$. For this reason, the proposed formulation (Equation (15)) proves to be a reliable and conservative tool for evaluating the q-factor of slender masonry structures under seismic excitation.

To solve the equation of motion, a simplification is adopted: for slender structures, the sine and cosine terms in Equation (1) are approximated using the first term of their Taylor series expansions; the result is Equation (3). However, the validity of this assumption depends on both the slenderness of the structure and the characteristics of the seismic

input. To investigate this, a dedicated MATLAB program is developed using the ODE45 solver to integrate the full nonlinear differential equation of motion without applying these simplifications (Equation (1)). The following figures present the results obtained for various values of the structure's slenderness and height, highlighting the influence of these parameters on the accuracy of the simplified model. The results are presented as the ratio between the rotation at the end of the seismic excitation ($t = t_{fin}$) and the slenderness as a function of the structure height H (Figure 6). This analysis is carried out for various values of slenderness and half-periods of the input accelerogram. The plots indicate that, for slender structures—identified using a limiting slenderness value of 0.25—the most significant variations occur at lower heights. These effects are more pronounced for higher slenderness values and longer accelerogram periods. The rotation values computed using Equation (1) are always lower than those obtained from Equation (3). For short structures (H = 1) and at the slenderness limit (α = 0.25), the reduction in final rotation reaches approximately 16%. However, this discrepancy becomes negligible for structure heights greater than 3, indicating a diminishing influence of the chosen formulation with increasing structural height. For these reasons, analyses based on Equation (3) systematically yield more conservative results, thus ensuring a higher margin of safety.

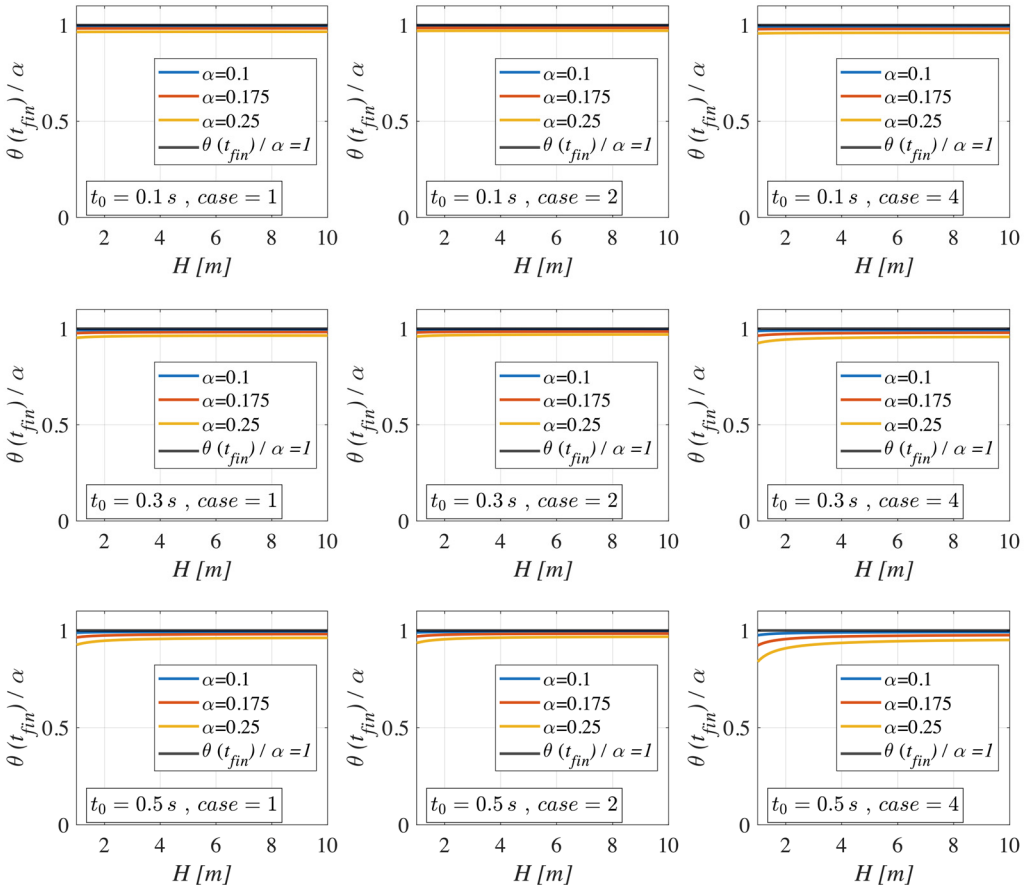

Figure 6. Comparison of the results from the integration of Equations (1) and (3).

3. Influence of the Number of Pulses

Seismic shaking is typically composed of a sequence of horizontal acceleration pulses with varying intensity, rather than a single, isolated pulse. To generalize this behavior, the seismic input can be idealized as a series of multiple pulses. In the present study, as in [10], a representative case of six consecutive pulses is considered (see Figure 7); collapse is assumed to occur at the onset of the seventh pulse, which induces a rotation exceeding

the slenderness of the masonry structure, thus triggering overturning. By imposing the collapse condition at the end of considered seismic excitation, the behavior factor decreases as the number of impulses increases [20]. This reduction stabilizes at the beginning of the 6 + 1 pulses (Figure 7). Considering the results obtained in the previous section, only seismic inputs corresponding to Cases 2 and 4 are selected for further analysis and comparison with those from Case 1, as previously reported by [26]. Following the procedure outlined by Coccia and Como [26], the resulting values for $q_{2-N=6+1}$ and $q_{4-N=6+1}$ are

$$q_{2-N=6+1}(x) = \frac{\frac{2}{3}(sinh(3pt_o))^2 + \frac{1}{3}}{(sinh(pt_o))^2 - \left(sinh\left(\frac{pt_o}{2}\right)\right)^2 + (sinh(2pt_o))^2 - (sinh(2.5pt_o))^2 - (sinh(1.5pt_o))^2 + \frac{2}{3}(sinh(3pt_o))^2} \quad (27)$$

and:

$$q_{4-N=6+1}(x) = \frac{\frac{2}{3}cosh(9pt_o)}{cosh(3pt_o) + cosh(6pt_o) - cosh(2pt_o) - cosh(8pt_o) + cosh(9pt_o) - cosh(5pt_o) + \frac{1}{3}} \quad (28)$$

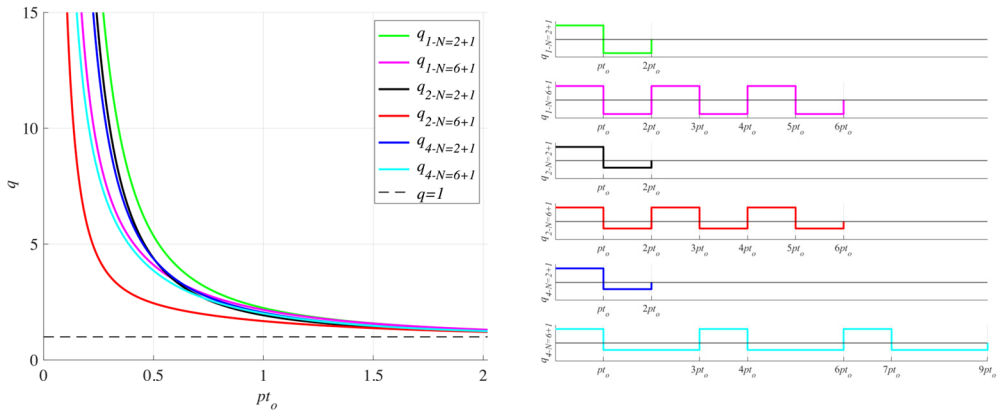

Figure 7. q-factor versus pt_o: influence of the number of pulse excitation.

As shown in Figure 7, which plots the behavior factors as a function of pt_o, the lowest q value corresponding to Equation (27) can be considered conservative for design purposes.

In Figure 8, the results obtained in this study (Equation (27) red curve) are compared with the results obtained with the procedure proposed by Makris et al. [9], illustrating that the behavior factor $q_{2-N=6+1}$ offers a safety margin, particularly for high w/p (= $\pi/(pt_o)$) ratios, which correspond to low pt_o values. The same figure includes the model proposed by Coccia and Como (blue curve) [26], allowing for a direct comparison with other established approaches.

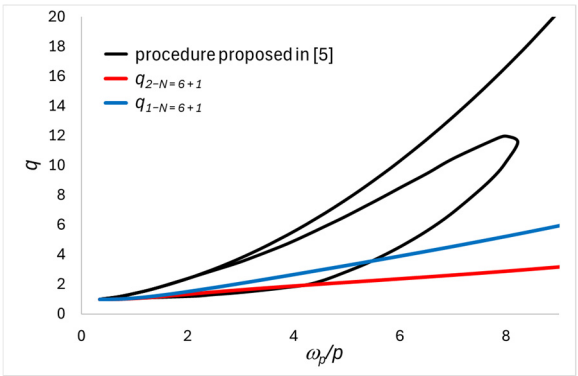

Figure 8. Comparison with the result obtained with the procedure proposed in [5].

4. Comparison Between Natural Accelerograms and Simple Input for the Earthquake

In this final section, a comparison is made between the proposed formulation of the behavior factor q and the results of a numerical investigation carried out using 20 natural Italian accelerograms. The reference structures have five different slenderness values, ranging from 0.05 to 0.25. The selected natural accelerograms, shown in Figure 9, are extracted from the ITACA database (https://itaca.mi.ingv.it/ItacaNet_40/#/home/, accessed on 24 June 2025). The main characteristics of the corresponding earthquakes appear in Table 1. The accelerograms are directly applied at the foundation level, assuming a rigid base without modeling soil–structure interactions or the effect of the local soil conditions on the input motion.

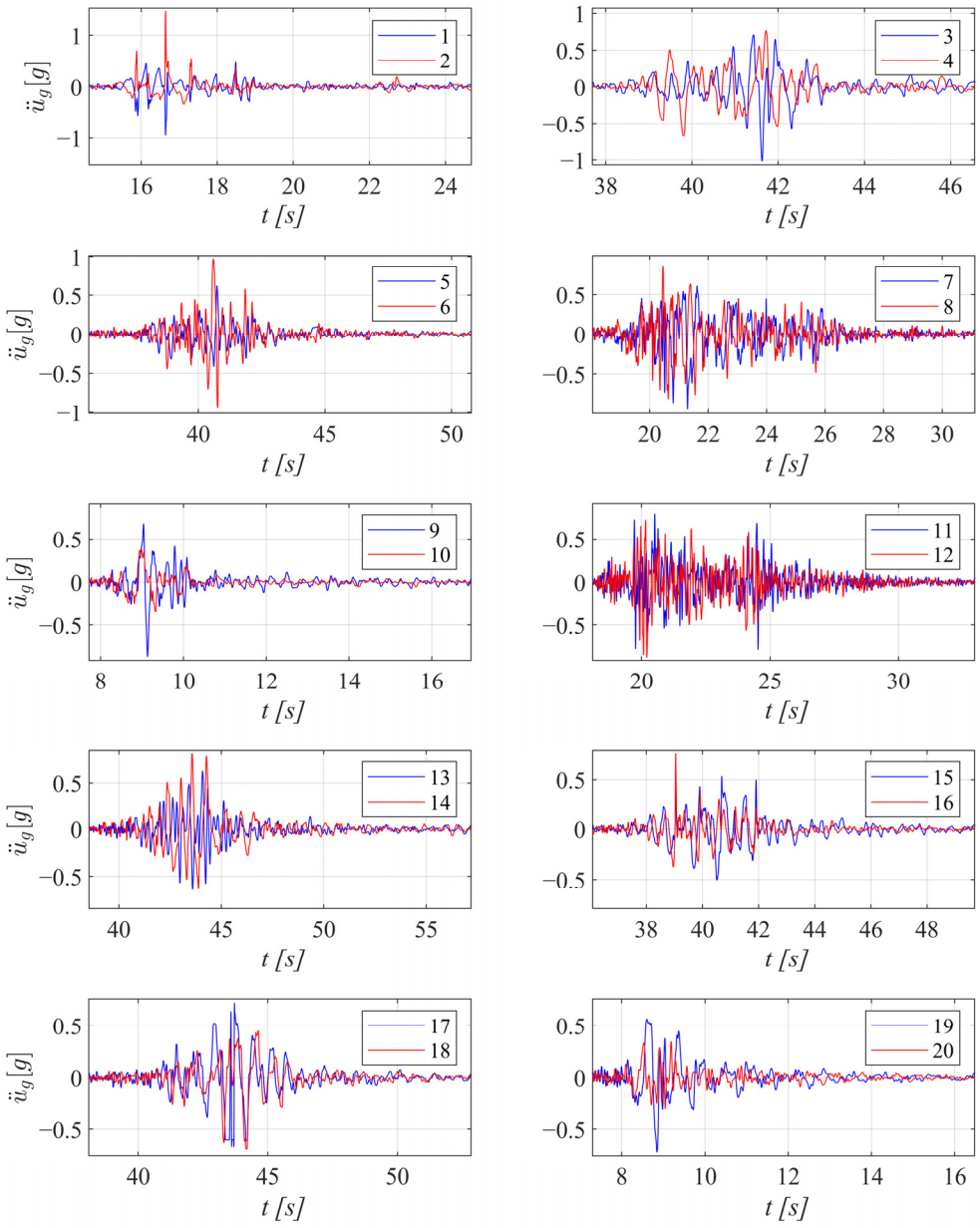

Figure 9. Natural Italian accelerograms from [43].

Table 1. Analyzed natural accelerograms and obtained results.

Case	PGA [cm/s^2]	PGV [cm/s]	Station	Date	Epicentral Distance [km]	Direction	Slenderness α									
							0.05		0.1		0.15		0.2		0.25	
							q	p	q	p	q	p	q	p	q	p
1	933.52	26.19	T1245	26 October 2016	7.1	E	19.03	1.9	9.52	2.91	6.34	3.81	4.76	3.59	3.81	4.64
2	1423.06	43.57				N	29.01	1.62	14.51	1.91	9.67	2.75	7.25	3.05	5.80	3.12
3	1001.65	55.04	MZ24	30 October 2016	24.4	E	20.42	1.22	10.21	2.12	6.81	1.87	5.11	2.39	4.08	2.46
4	747.74	−73.6				N	15.24	1.2	7.62	1.42	5.08	1.66	3.81	1.58	3.05	1.91
5	612.63	−40.98	MZ51	30 October 2016	25.9	E	12.49	1.5	6.24	1.83	4.16	1.65	3.12	1.71	2.50	1.96
6	947.25	−74.98				N	19.31	0.95	9.66	1.19	6.44	1.91	4.83	2.51	3.86	2.41
7	931.14	77.3	FCC	30 October 2016	10.9	E	18.98	0.8	9.49	1.64	6.33	1.57	4.75	2.91	3.80	3.51
8	843.73	−37.81				N	17.20	1.06	8.60	2	5.73	2.93	4.30	3.14	3.44	3.26
9	850.8	43.55	AMT	24 August 2016	8.5	E	17.35	1.94	8.67	3.25	5.78	4.43	4.34	4.31	3.47	3.76
10	368.39	−41.5				N	7.51	2.01	3.76	2.65	2.50	2.87	1.88	4.2	1.50	5.24
11	779.27	−60.73	T1213	30 October 2016	12.6	E	15.89	1.02	7.94	1.81	5.30	1.93	3.97	1.9	3.18	2.33
12	849.97	−30.54				N	17.33	1.58	8.66	1.8	5.78	2.15	4.33	3.1	3.47	4.24
13	633.77	50.08	MZ04	30 October 2016	23	E	12.92	1.41	6.46	1.62	4.31	2.46	3.23	2.38	2.58	2.29
14	793.29	−85.39				N	16.17	0.8	8.09	1.53	5.39	2.02	4.04	1.82	3.23	2.29
15	668.61	50.91	MZ28	30 October 2016	28.4	E	13.63	1.17	6.82	2	4.54	2.3	3.41	3.41	2.73	4.03
16	741.31	28.93				N	15.11	1.91	7.56	3.06	5.04	3.01	3.78	3.61	3.02	4.41
17	707.01	92.22	MZ12	30 October 2016	27.1	E	14.41	0.78	7.21	0.96	4.80	1.09	3.60	1.36	2.88	1.72
18	672.93	67.79				E	13.72	1.41	6.86	1.47	4.57	2.2	3.43	3.31	2.74	2.81
19	706.8	55.7	CMI	30 October 2016	5.7	N	14.41	1.91	7.20	2.2	4.80	2.39	3.60	3.61	2.88	3.72
20	334.77	18.62				E	6.83	2.99	3.41	3.84	2.28	4.19	1.71	6.5	1.37	5.36

The numerical integration of the motion's differential equation is performed using a MATLAB code that employs the ODE45 solver. The ODE45 solver, based on an explicit Runge–Kutta method, is selected for its robustness and efficiency in solving non-stiff, nonlinear ordinary differential equations, such as those governing rocking motion. The computational cost remains very low due to the limited duration of each simulation and the simplicity of the dynamic model. Convergence is verified by varying solver tolerances, and stable results are obtained for a relative tolerance of 1×10^{-6}.

To avoid scaling the natural accelerograms, the pulsation p that causes the collapse of the structure is treated as an unknown variable. For each combination of slenderness and accelerogram, the q-factor is computed using Equation (27), and the corresponding results are reported in Table 1. At the same time, the pulsation gradually increases until collapse occurs.

The period t_o is defined as half of the earthquake period T_p. The identification of this parameter is carried out using different approaches. In particular, t_o is defined as

- t_{o_1}: the distance between the two points of zero acceleration delimiting the maximum (positive or negative) area A_{max} of the impulse (Figure 10a), as in [10];

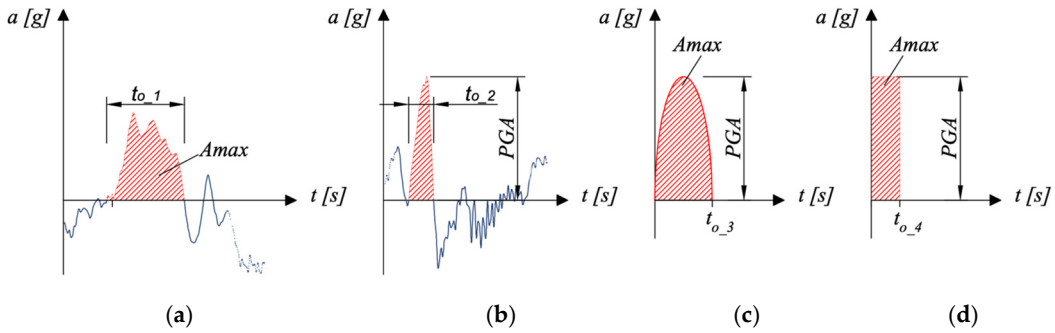

Figure 10. The evaluation of the half-period of the accelerogram: (**a**) t_{o_1}; (**b**) t_{o_2}; (**c**) t_{o_3} and (**d**) t_{o_4}.

- t_{o_2}: the duration of the impulse characterized by the maximum acceleration intensity PGA (Figure 10b), as in [10];

- t_{o_3} is evaluated considering a sinusoidal wave having the same PGA and the same area A_{max} of the accelerogram (Figure 10c), as in [10]:

$$t_{o\_3} = \frac{A_{max}\pi}{2PGA} \tag{29}$$

- t_{o_4} is evaluated considering a constant wave having the same PGA and the same area A_{max} of the accelerogram (Figure 10d), as in [10]:

$$t_{o\_4} = \frac{A_{max}}{PGA} \tag{30}$$

- t_{o_5} is evaluated as half of the inverse of the frequency of an equivalent harmonic wave [44]:

$$t_{o\_5} = \frac{\pi\ PGV}{PGA} \tag{31}$$

- t_{o_6} is equal to half the inverse of the frequency that maximizes the Fourier amplitude spectra of ground acceleration time-history (the results are reported in Appendix A);
- t_{o_7} is equal to half the inverse of the frequency that maximizes the Fourier amplitude spectra of ground velocity time-history (the results are reported in Appendix A);
- t_{o_8} and t_{o_10} are equal to half the inverse of the frequencies that maximize the amplitude or the total energy, respectively, of the wavelet analysis considering the ground acceleration time-history (the results are reported in Appendix A);
- t_{o_9} and t_{o_11} are equal to half the inverse of the frequencies that maximize the mean amplitude or the total energy, respectively, of the wavelet analysis considering the ground velocity time-history (the results are reported in Appendix A).

Fourier analysis represents a signal of infinite duration and single-frequency content as a linear combination of sine and cosine waves. In contrast, wavelet analysis decomposes a signal into wavelets that are localized in both time and frequency, allowing for the representation of transient or non-stationary behavior. In the numerical analysis carried out, the chosen mother wavelet is the Morse wavelet, which offers flexibility in controlling time–frequency localization through its shape parameters. This makes it particularly suitable for analyzing seismic signals, which typically exhibit both sharp transient and frequency content varying over time.

In the Morse wavelet mother function,

$$\Psi = \mathrm{U}(\omega)\omega^{\beta}e^{-\omega^{\gamma}} \tag{32}$$

as in [35], the parameters β and γ are chosen equal to 27 and 3, respectively.

The values of the half-period t_o, evaluated according to the previously defined criteria, are reported in Table 2. Finally, the results are plotted in Figure 11, along with the curve representing the q-factor as evaluated using Equation (27). For a simplified estimation of the earthquake's half-period, the parameter t_{o_5} can be employed in Equation (27) for defining the behavior factor. This parameter is straightforward to compute from an accelerogram and, in nearly all the cases analyzed, the resulting formulation provides a conservative (i.e., safe) estimate for structural verification. In Figure 12, only this case is plotted, along with the line q = 2, which corresponds to the minimum requirement prescribed by the Italian building code for out-of-plane collapse verification [45]. For pt_o values greater than 0.7, the design value provided by the Italian standard is not conservative.

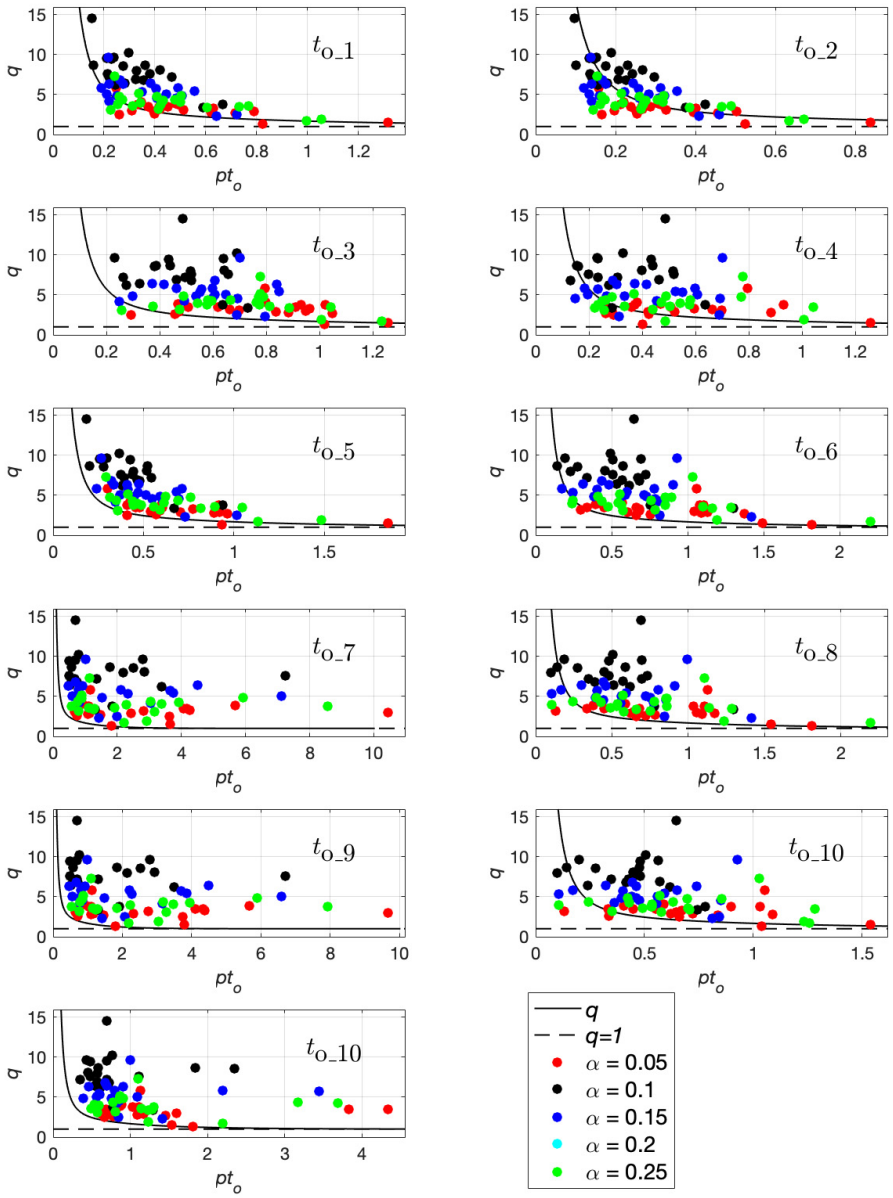

Figure 11. Comparison between the proposed formulation and the results obtained from natural accelerogram records.

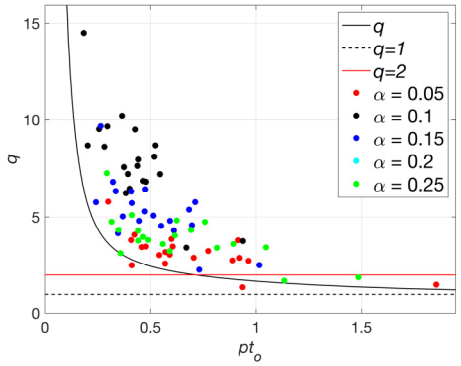

Figure 12. q-factor versus pt_o: proposed formation: q Equation (27), t_o Equation (31), and p Equation (4).

Table 2. Half period of the earthquake (evaluated in s).

Case	t_{o_1}	t_{o_2}	t_{o_3}	t_{o_4}	t_{o_5}	t_{o_6}	t_{o_7}	t_{o_8}	t_{o_9}	t_{o_10}	t_{o_11}
1	0.072	0.046	0.220	0.080	0.088	0.238	0.238	0.239	0.239	0.194	0.239
2	0.079	0.051	0.255	0.255	0.096	0.339	0.370	0.362	0.362	0.338	0.362
3	0.141	0.090	0.325	0.155	0.173	0.232	0.369	0.239	0.362	0.239	0.362
4	0.268	0.171	0.365	0.365	0.309	0.357	0.357	0.338	0.338	0.338	0.338
5	0.133	0.085	0.150	0.150	0.210	0.337	1.847	0.338	1.910	0.338	0.338
6	0.200	0.127	0.195	0.195	0.249	0.163	2.360	0.157	2.351	0.169	0.362
7	0.140	0.089	0.265	0.265	0.261	0.308	0.308	0.294	0.294	0.294	0.294
8	0.138	0.088	0.190	0.080	0.141	0.139	1.250	0.137	1.260	0.137	1.176
9	0.111	0.071	0.135	0.135	0.161	0.177	0.177	0.181	0.181	0.147	0.181
10	0.251	0.160	0.240	0.240	0.354	0.285	0.697	0.294	0.724	0.294	0.294
11	0.181	0.115	0.285	0.285	0.245	0.127	1.208	0.056	1.176	0.056	0.315
12	0.088	0.056	0.215	0.085	0.113	0.080	0.984	0.079	1.023	0.079	1.023
13	0.174	0.111	0.200	0.185	0.248	0.329	0.329	0.315	0.315	0.147	0.338
14	0.276	0.175	0.420	0.260	0.338	0.298	1.858	0.294	1.910	0.294	0.294
15	0.177	0.113	0.260	0.065	0.239	0.341	0.369	0.194	0.362	0.208	0.362
16	0.070	0.045	0.215	0.065	0.123	0.237	2.368	0.239	2.194	0.147	0.362
17	0.231	0.147	0.275	0.245	0.410	0.352	1.406	0.362	1.350	0.362	0.362
18	0.221	0.141	0.315	0.315	0.316	0.388	0.388	0.388	0.388	0.388	0.388
19	0.212	0.135	0.225	0.140	0.248	0.305	0.305	0.315	0.315	0.194	0.315
20	0.154	0.098	0.190	0.075	0.174	0.339	0.339	0.338	0.338	0.194	0.338

5. Conclusions

This study presents a closed-form analytical formulation for evaluating the behavior factor (q-factor) associated with overturning collapse of slender masonry structures subjected to out-of-plane seismic excitation. The analytical model assumes a perfectly rigid block and neglects base sliding, which simplifies the dynamic response to pure rocking. This assumption is valid primarily for slender masonry elements ($\alpha < 0.25$), where rocking dominates and sliding is typically negligible. The approach is grounded in a simplified rocking model, where the collapse condition is defined as the attainment of a rotation equal to the structure's slenderness at the end of the seismic input. Five distinct idealized seismic pulses are considered, and the influence of pulse sequences is explored to reflect more realistic seismic demand scenarios. The analytical results are validated by comparison with the outcomes of numerical integration of the equation of motion, performed using a set of 20 natural ground motion records from Italian earthquakes. This comparison also aims to identify the most suitable definition of the seismic period for use within the analytical framework. Among the different definitions of the period, the inverse of the frequency of an equivalent harmonic wave showed the best agreement with numerical. The proposed formulation provides an efficient and reliable tool for the simplified seismic assessment of slender unreinforced masonry structures. Due to its conservative nature, the method is well-suited for implementation within performance-based design approaches and code-based verification procedures for out-of-plane failure mechanisms. Nevertheless, the model presents some limitations. It assumes idealized boundary conditions and neglects base sliding, frictional effects, and geometric or material imperfections. Future research should aim to refine the model by incorporating sliding failure and geometric or material imperfection, as well as validating it against a broader database of recorded or synthetic accelerograms.

Funding: This research received no external funding.

Data Availability Statement: The data supporting the conclusions of this article will be made available by the author upon request.

Conflicts of Interest: The author declares no conflicts of interest.

Appendix A

Frequency in the Fourier amplitude spectra (FFT) and predominant and dominant frequencies in the wavelet analysis (CWT).

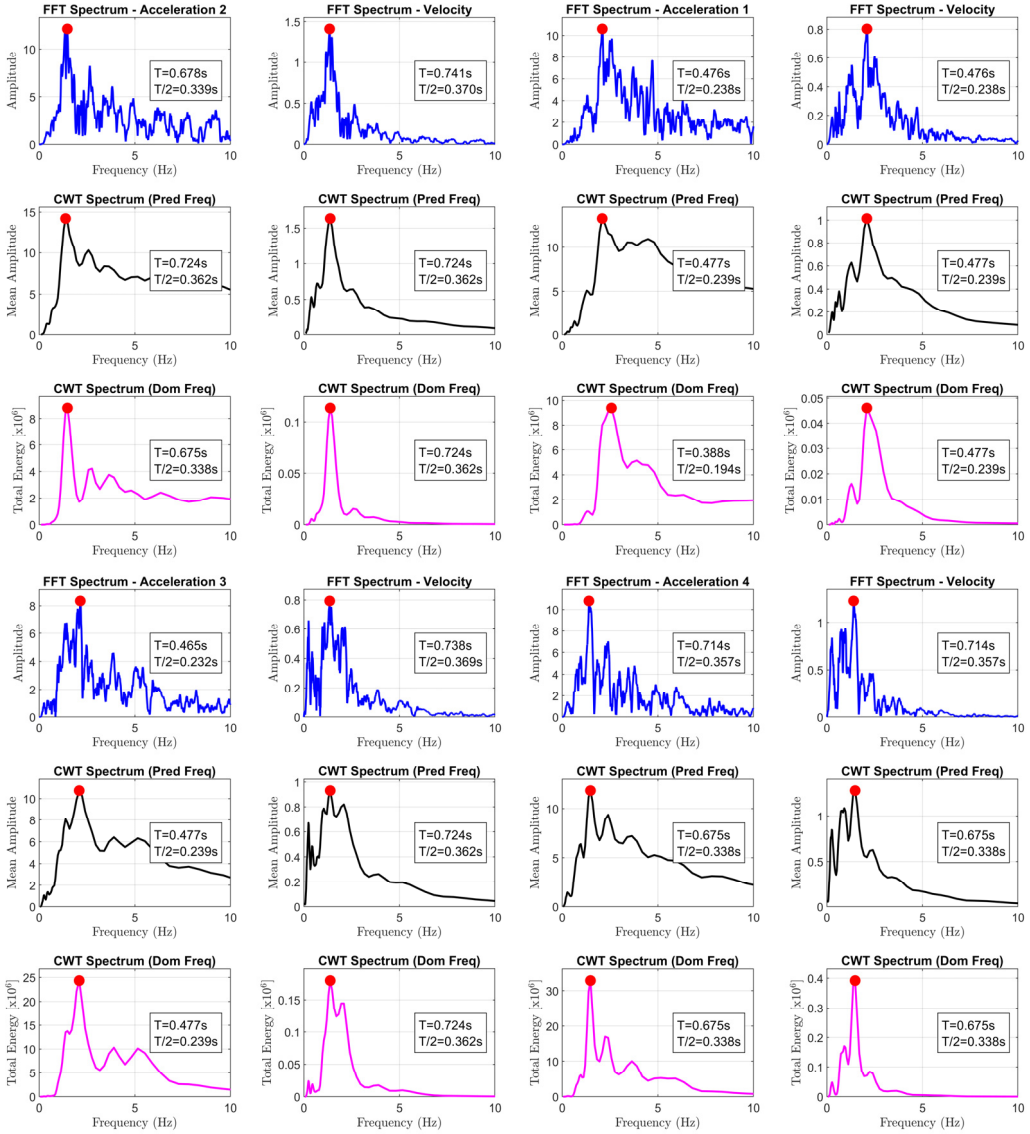

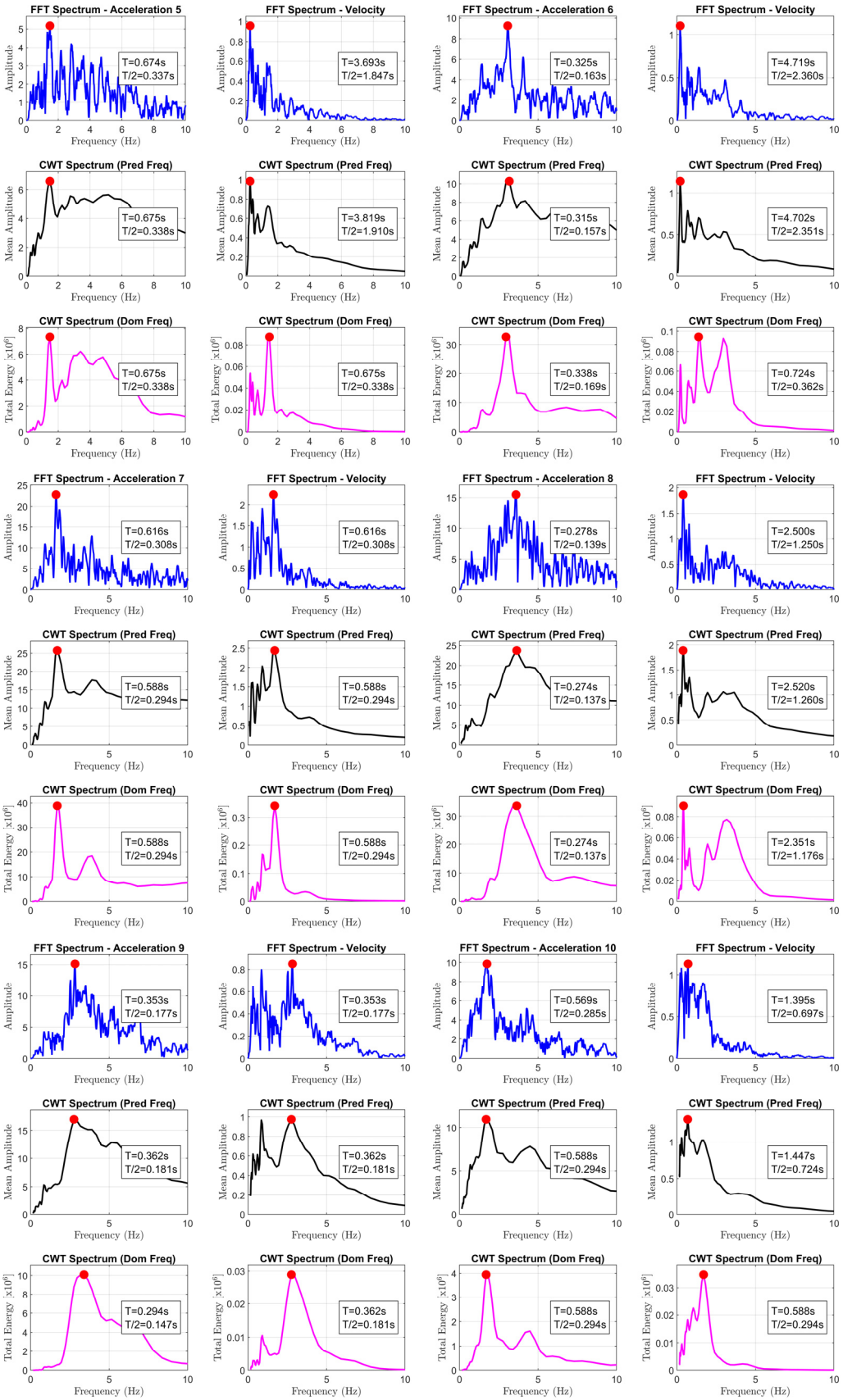
FFT Spectrum - Acceleration 5
T=0.674s
T/2=0.337s
FFT Spectrum - Velocity
T=3.693s
T/2=1.847s
FFT Spectrum - Acceleration 6
T=0.325s
T/2=0.163s
FFT Spectrum - Velocity
T=4.719s
T/2=2.360s
CWT Spectrum (Pred Freq)
T=0.675s
T/2=0.338s
CWT Spectrum (Pred Freq)
T=3.819s
T/2=1.910s
CWT Spectrum (Pred Freq)
T=0.315s
T/2=0.157s
CWT Spectrum (Pred Freq)
T=4.702s
T/2=2.351s
CWT Spectrum (Dom Freq)
T=0.675s
T/2=0.338s
CWT Spectrum (Dom Freq)
T=0.675s
T/2=0.338s
CWT Spectrum (Dom Freq)
T=0.338s
T/2=0.169s
CWT Spectrum (Dom Freq)
T=0.724s
T/2=0.362s
FFT Spectrum - Acceleration 7
T=0.616s
T/2=0.308s
FFT Spectrum - Velocity
T=0.616s
T/2=0.308s
FFT Spectrum - Acceleration 8
T=0.278s
T/2=0.139s
FFT Spectrum - Velocity
T=2.500s
T/2=1.250s
CWT Spectrum (Pred Freq)
T=0.588s
T/2=0.294s
CWT Spectrum (Pred Freq)
T=0.588s
T/2=0.294s
CWT Spectrum (Pred Freq)
T=0.274s
T/2=0.137s
CWT Spectrum (Pred Freq)
T=2.520s
T/2=1.260s
CWT Spectrum (Dom Freq)
T=0.588s
T/2=0.294s
CWT Spectrum (Dom Freq)
T=0.588s
T/2=0.294s
CWT Spectrum (Dom Freq)
T=0.274s
T/2=0.137s
CWT Spectrum (Dom Freq)
T=2.351s
T/2=1.176s
FFT Spectrum - Acceleration 9
T=0.353s
T/2=0.177s
FFT Spectrum - Velocity
T=0.353s
T/2=0.177s
FFT Spectrum - Acceleration 10
T=0.569s
T/2=0.285s
FFT Spectrum - Velocity
T=1.395s
T/2=0.697s
CWT Spectrum (Pred Freq)
T=0.362s
T/2=0.181s
CWT Spectrum (Pred Freq)
T=0.362s
T/2=0.181s
CWT Spectrum (Pred Freq)
T=0.588s
T/2=0.294s
CWT Spectrum (Pred Freq)
T=1.447s
T/2=0.724s
CWT Spectrum (Dom Freq)
T=0.294s
T/2=0.147s
CWT Spectrum (Dom Freq)
T=0.362s
T/2=0.181s
CWT Spectrum (Dom Freq)
T=0.588s
T/2=0.294s
CWT Spectrum (Dom Freq)
T=0.588s
T/2=0.294s
Amplitude
Mean Amplitude
Total Energy |x10⁶|
Frequency (Hz)

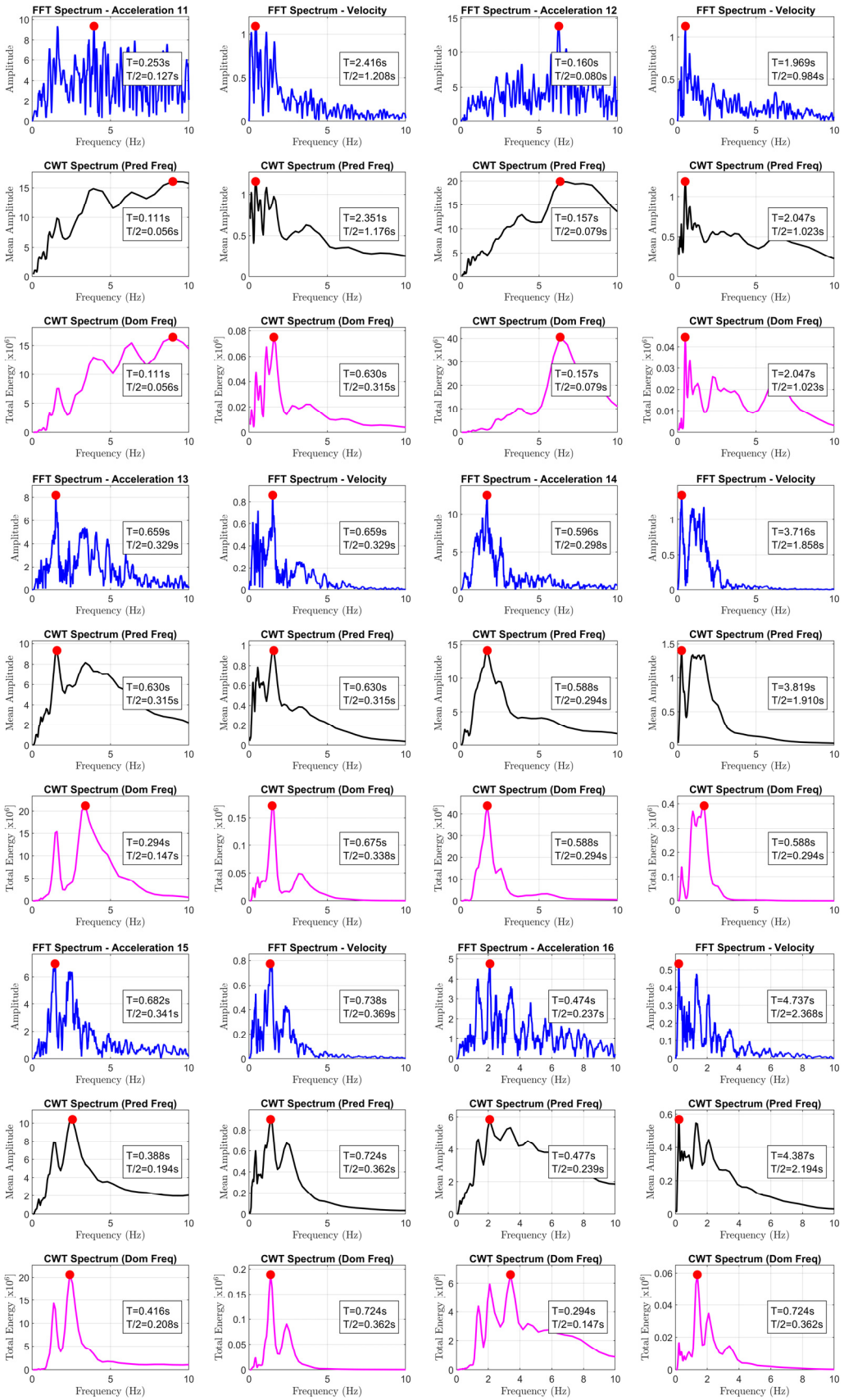
FFT Spectrum - Acceleration 11
T=0.253s
T/2=0.127s
FFT Spectrum - Velocity
T=2.416s
T/2=1.208s
FFT Spectrum - Acceleration 12
T=0.160s
T/2=0.080s
FFT Spectrum - Velocity
T=1.969s
T/2=0.984s
CWT Spectrum (Pred Freq)
T=0.111s
T/2=0.056s
CWT Spectrum (Pred Freq)
T=2.351s
T/2=1.176s
CWT Spectrum (Pred Freq)
T=0.157s
T/2=0.079s
CWT Spectrum (Pred Freq)
T=2.047s
T/2=1.023s
CWT Spectrum (Dom Freq)
T=0.111s
T/2=0.056s
CWT Spectrum (Dom Freq)
T=0.630s
T/2=0.315s
CWT Spectrum (Dom Freq)
T=0.157s
T/2=0.079s
CWT Spectrum (Dom Freq)
T=2.047s
T/2=1.023s
FFT Spectrum - Acceleration 13
T=0.659s
T/2=0.329s
FFT Spectrum - Velocity
T=0.659s
T/2=0.329s
FFT Spectrum - Acceleration 14
T=0.596s
T/2=0.298s
FFT Spectrum - Velocity
T=3.716s
T/2=1.858s
CWT Spectrum (Pred Freq)
T=0.630s
T/2=0.315s
CWT Spectrum (Pred Freq)
T=0.630s
T/2=0.315s
CWT Spectrum (Pred Freq)
T=0.588s
T/2=0.294s
CWT Spectrum (Pred Freq)
T=3.819s
T/2=1.910s
CWT Spectrum (Dom Freq)
T=0.294s
T/2=0.147s
CWT Spectrum (Dom Freq)
T=0.675s
T/2=0.338s
CWT Spectrum (Dom Freq)
T=0.588s
T/2=0.294s
CWT Spectrum (Dom Freq)
T=0.588s
T/2=0.294s
FFT Spectrum - Acceleration 15
T=0.682s
T/2=0.341s
FFT Spectrum - Velocity
T=0.738s
T/2=0.369s
FFT Spectrum - Acceleration 16
T=0.474s
T/2=0.237s
FFT Spectrum - Velocity
T=4.737s
T/2=2.368s
CWT Spectrum (Pred Freq)
T=0.388s
T/2=0.194s
CWT Spectrum (Pred Freq)
T=0.724s
T/2=0.362s
CWT Spectrum (Pred Freq)
T=0.477s
T/2=0.239s
CWT Spectrum (Pred Freq)
T=4.387s
T/2=2.194s
CWT Spectrum (Dom Freq)
T=0.416s
T/2=0.208s
CWT Spectrum (Dom Freq)
T=0.724s
T/2=0.362s
CWT Spectrum (Dom Freq)
T=0.294s
T/2=0.147s
CWT Spectrum (Dom Freq)
T=0.724s
T/2=0.362s
Frequency (Hz)
Amplitude
Mean Amplitude
Total Energy (x10^6)

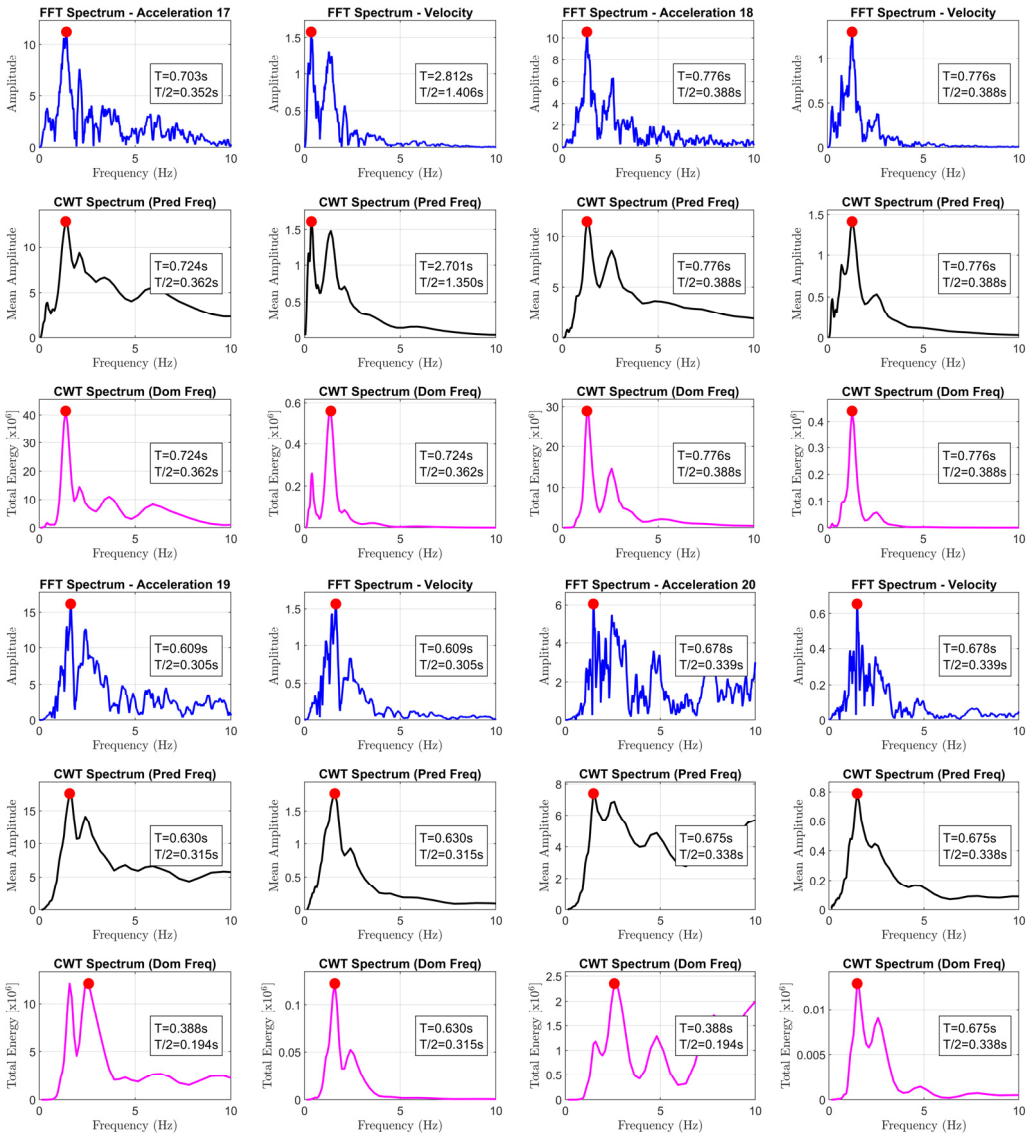

References

1. Bernardo, V.; Campos Costa, A.; Lourenço, P.B. Stochastic-based vulnerability curves for the out-of-plane seismic safety assessment of URM walls. *Bull. Earthq. Eng.* **2024**, *22*, 435–459. [CrossRef]
2. Ghezelbash, A.; Sharma, S.; D'Altri, A.M.; Lourenço, P.B.; Rots, J.G.; Messali, F. Challenges in High-Fidelity Implicit Block-Based Numerical Simulation of Dynamic Out-of-Plane Two-Way Bending in Unreinforced Brick Masonry Walls. *Earthq. Eng. Struct. Dyn.* **2025**, *54*, 1836–1858. [CrossRef]
3. Mazzeo, M.; Laudani, R.; Santoro, R. Uncertainty effect on seismic capacity assessment in the out-of-plane failure mechanisms of masonry structures by probabilistic and non-probabilistic approaches. *Dev. Built Environ.* **2024**, *17*, 100366. [CrossRef]
4. Manikandan, K.; Nidhi, M.; Micelli, F.; Cascardi, A.; Sivasubramanian, M.V. Seismic vulnerability assessment of slender masonry structures: A machine learning approach with vibration-based assessment and nonlinear dynamic analysis. *Structures* **2025**, *79*, 109272. [CrossRef]
5. De Felice, G. Out-of-plane seismic capacity of masonry depending on wall section morphology. *Int. J. Archit. Herit.* **2011**, *5*, 466–482. [CrossRef]
6. Housner, G.W. The behavior of inverted pendulum structures during earthquakes. *Bull. Seismol. Soc. Am.* **1963**, *53*, 403–417. [CrossRef]
7. Yim, C.S.; Chopra, A.K.; Penzien, J. Rocking response of rigid blocks to earthquakes. *Earthq. Eng. Struct. Dyn.* **1980**, *8*, 565–587. [CrossRef]
8. Aslam, M.; Godden, W.G.; Scalise, D.T. Earthquake rocking response of rigid bodies. *J. Struct. Div.* **1980**, *106*, 377–392. [CrossRef]
9. Makris, N.; Kampas, G. Size versus slenderness: Two competing parameters in the seismic stability of free-standing rocking columns. *Bull. Seismol. Soc. Am.* **2016**, *106*, 104–122. [CrossRef]

10. Coccia, S.; Como, M.; Di Carlo, F. The slender rigid block: Archetype for the seismic analysis of masonry structures. *J. Earthq. Eng.* **2023**, *27*, 2630–2654. [CrossRef]
11. Makris, N.; Roussos, Y. *Rocking Response and Overturning of Equipment Under Horizontal Pulse-Type Motions*; Pacific Earthquake Engineering Research Center: Berkeley, CA, USA, 1998.
12. Zhang, J.; Makris, N. Rocking response of free-standing blocks under cycloidal pulses. *J. Eng. Mech.* **2001**, *127*, 473–483. [CrossRef]
13. Kounadis, A.N. On the overturning instability of a rectangular rigid block under ground excitation. *Open Mech. J.* **2010**, *4*, 43–57. [CrossRef]
14. Hao, H.; Zhou, Y. Rigid structure response analysis to seismic and blast induced ground motions. *Procedia Eng.* **2011**, *14*, 946–955. [CrossRef]
15. Dimitrakopoulos, E.G.; Fung, E.D.W. Closed-form rocking overturning conditions for a family of pulse ground motions. *Proc. R. Soc. A Math. Phys. Eng. Sci.* **2016**, *472*, 20160662. [CrossRef] [PubMed]
16. Voyagaki, E.; Psycharis, I.N.; Mylonakis, G. Complex response of a rocking block to a full-cycle pulse. *J. Eng. Mech.* **2014**, *140*, 04014024-1–04014024-15. [CrossRef]
17. Nabeshima, K.; Taniguchi, R.; Kojima, K.; Takewaki, I. Closed-form overturning limit of rigid block under critical near-fault ground motions. *Front. Built Environ.* **2016**, *2*, 9. [CrossRef]
18. Taniguchi, R.; Nabeshima, K.; Kojima, K.; Takewaki, I. Closed-form rocking vibration of rigid block under critical and non-critical double impulse. *Int. J. Earthq. Impact Eng.* **2017**, *2*, 32–45. [CrossRef]
19. Dimitrakopoulos, E.G.; DeJong, M.J. Revisiting the rocking block: Closed-form solutions and similarity laws. *Proc. R. Soc. A Math. Phys. Eng. Sci.* **2012**, *468*, 2294–2318. [CrossRef]
20. Coccia, S.; Como, M. A new theory of the dynamical collapse of no-tension structures under sequences of pulses of horizontal acceleration. *Meccanica* **2025**, 1–14. [CrossRef]
21. Coccia, S.; Di Carlo, F.; Imperatore, S. Force reduction factor for out-of-plane simple mechanisms of masonry structures. *Bull. Earthq. Eng.* **2017**, *15*, 1241–1259. [CrossRef]
22. Psycharis, I.N.; Papastamatiou, D.Y.; Alexandris, A.P. Parametric investigation of the stability of classical columns under harmonic and earthquake excitations. *Earthq. Eng. Struct. Dyn.* **2000**, *29*, 1093–1109. [CrossRef]
23. Spanos, P.D.; Roussis, P.C.; Politis, N.P.A. Dynamic analysis of stacked rigid blocks. *Soil Dyn. Earthq. Eng.* **2001**, *21*, 559–578. [CrossRef]
24. Ther, T.; Kollár, L.P. Model for multiblock columns subjected to base excitation. *Earthq. Eng. Struct. Dyn.* **2018**, *47*, 418–437. [CrossRef]
25. Como, M.; Di Carlo, F.; Coccia, S. Dynamic response of rocking cracked masonry walls. *Meccanica* **2019**, *54*, 381–398. [CrossRef]
26. Coccia, S.; Como, M. Out-of-Plane Dynamical Strength of Masonry Walls Under Seismic Actions. *J. Earthq. Eng.* **2024**, *28*(4), 1040–1068. [CrossRef]
27. Destro Bisol, G.; Prajapati, S.; Sorrentino, L.; AlShawa, O. Vertical spanning wall elastically restrained at the top: Validation and parametric dynamic analysis. *Bull. Earthq. Eng.* **2024**, *22*, 3951–3978. [CrossRef]
28. Oppenheim, I.J. The masonry arch as a four-link mechanism under base motion. *Earthq. Eng. Struct. Dyn.* **1992**, *21*, 1005–1017. [CrossRef]
29. De Lorenzis, L.; DeJong, M.; Ochsendorf, J. Failure of masonry arches under impulse base motion. *Earthq. Eng. Struct. Dyn.* **2007**, *36*, 2119–2136. [CrossRef]
30. Carlo, F.D.; Coccia, S.; Piedigrossi, M. Dynamics of masonry pointed arches under base motion. *Int. J. Mason. Res. Innov.* **2017**, *2*, 335–354. [CrossRef]
31. Coccia, S.; Como, M. Dynamical Collapse of Masonry Arches Under Sequences of Impulses of Horizontal Acceleration. *J. Earthq. Eng.* **2024**, *28*, 4644–4671. [CrossRef]
32. Bisegna, P.; Coccia, S.; Como, M.; Nodargi, N.A. A novel impact model for the rocking motion of masonry arches. *Meccanica* **2023**, *58*, 2079–2093. [CrossRef]
33. Giresini, L. Effect of dampers on the seismic performance of masonry walls assessed through fragility and demand hazard curves. *Eng. Struct.* **2022**, *261*, 114295. [CrossRef]
34. Nodargi, N.A.; Bisegna, P. Seismic fragility of free-standing rocking-sliding rigid blocks under earthquake excitation. *Meccanica* **2025**, 1–25. [CrossRef]
35. Giresini, L.; Solarino, F.; AlShawa, O. Dissipative tie-rods restraining one-sided rocking masonry walls: Analytical formulation and experimental tests. *Bull. Earthq. Eng.* **2025**, *23*, 779–804. [CrossRef]
36. Lv, Y.; Liu, P.; Li, F. Rocking responses of free-standing rigid blocks on flexible foundation with a slope under earthquakes: Structure-foundation interaction effects. *J. Vibroeng.* **2025**, *27*, 462–478. [CrossRef]
37. Destro Bisol, G.; DeJong, M.J.; Liberatore, D.; Sorrentino, L. Displacement-based design procedures for rigid block isolation. *Earthq. Eng. Struct. Dyn.* **2024**, *53*, 1552–1572. [CrossRef]

38. Casapulla, C.; Giresini, L.; Argiento, L.U.; Maione, A. Nonlinear static and dynamic analysis of rocking masonry corners using rigid macro-block modeling. *Int. J. Struct. Stab. Dyn.* **2019**, *19*, 1950137. [CrossRef]
39. Mavroeidis, G.P.; Dong, G.; Papageorgiou, A.S. Near-fault ground motions, and the response of elastic and inelastic single-degree-of-freedom (SDOF) systems. *Earthq. Eng. Struct. Dyn.* **2004**, *33*, 1023–1049. [CrossRef]
40. Pelekis, I.; Madabhushi, G.S.; DeJong, M.J. Soil behaviour beneath buildings with structural and foundation rocking. *Soil Dyn. Earthq. Eng.* **2019**, *123*, 48–63. [CrossRef]
41. *MATLAB, Version R2024b*; The MathWorks Inc.: Natick, MA, USA, 2024.
42. Várkonyi, P.L.; Kocsis, M.; Ther, T. Rigid impacts of three-dimensional rocking structures. *Nonlinear Dyn.* **2022**, *107*, 1839–1858. [CrossRef]
43. D'Amico, M.; Felicetta, C.; Russo, E.; Sgobba, S.; Lanzano, G.; Pacor, F.; Luzi, L. The new Italian accelerometric archive ITACA: Database, web-services, and tools to access and analyze earthquakes waveforms. *Rapp. Tec. INGV* 2021. [CrossRef]
44. Kramer, S.L. *Geotechnical Earthquake Engineering*; Prentice Hall: New York, NY, USA, 1996; p. 794.
45. delle Infrastrutture, M. Istruzioni per l'applicazione delle nuove norme tecniche per le costruzioni di cui al decreto ministeriale 14 gennaio 2008. *Supplemento ordinario n. 27 alla Gazzetta Ufficiale 26 febbraio* **2009**, *47*, 229–392.